Antiferromagnetism at $T > 500\,\mathrm{K}$ in the layered hexagonal ruthenate SrRu$_2$O$_6$

C. I. Hiley,[1] D. O. Scanlon,[2,3] A. A. Sokol,[2] S. M. Woodley,[2] A. M. Ganose,[2,3] S. Sangiao,[4] J. M. De Teresa,[4] P. Manuel,[5]
D. D. Khalyavin,[5] M. Walker,[6] M. R. Lees,[6] and R. I. Walton[1,*]

[1]*Department of Chemistry, University of Warwick, Gibbet Hill Road, Coventry CV4 7AL, United Kingdom*
[2]*University College London, Kathleen Lonsdale Materials Chemistry, Department of Chemistry, 20 Gordon Street,*
London WC1H 0AJ, United Kingdom
[3]*Diamond Light Source, Ltd., Diamond House, Harwell Science and Innovation Campus, Didcot, Oxfordshire OX11 0DE, United Kingdom*
[4]*Insituto de Nanociencia de Aragón (INA), Universidad de Zaragoza, Zaragoza, Spain*
[5]*ISIS Facility, Rutherford Appleton Laboratory, Harwell Science and Innovation Campus, Didcot, Oxfordshire OX11 0QX, United Kingdom*
[6]*Department of Physics, University of Warwick, Gibbet Hill Road, Coventry CV4 7AL, United Kingdom*

We report an experimental and computational study of the magnetic and electronic properties of the layered Ru(V) oxide SrRu$_2$O$_6$ (hexagonal, $P\bar{3}1m$), which shows antiferromagnetic order with a Néel temperature of 563(2) K, among the highest for $4d$ oxides. Magnetic order occurs both within edge-shared octahedral sheets and between layers and is accompanied by anisotropic thermal expansivity that implies strong magnetoelastic coupling of Ru(V) centers. Electrical transport measurements using focused-ion-beam–induced deposited contacts on a micron-scale crystallite as a function of temperature show p-type semiconductivity. The calculated electronic structure using hybrid density functional theory successfully accounts for the experimentally observed magnetic and electronic structure, and Monte Carlo simulations reveal how strong intralayer as well as weaker interlayer interactions are a defining feature of the high-temperature magnetic order in the material.

I. INTRODUCTION

The diverse magnetic and electronic properties of the Sr–Ru–O system have been widely investigated, particularly for Ru(IV) oxides. SrRuO$_3$ is a rare example of a $4d$ ferromagnetic oxide [1], which is also a metallic conductor below its Curie temperature (160 K) [2]. Sr$_{n+1}$Ru$_n$O$_{3n+1}$ Ruddlesden-Popper phases include the spin-triplet chiral superconductor Sr$_2$RuO$_4$ [3], Sr$_3$Ru$_2$O$_7$, an itinerant metamagnet [4] with electron nematic behavior [5], and Sr$_4$Ru$_3$O$_{10}$, an itinerant ferromagnet and metamagnet [6,7]. While some strontium ruthenates contain Ru in the $+5$ or the $+6$ oxidation state, for example, Sr$_2$Ru$_2^{\mathrm{V}}$Ru$^{\mathrm{VI}}$O$_{10}$ [8], Sr$_4$Ru$_2^{\mathrm{V}}$O$_9$ [9], and Sr$_4$Ru$_2^{\mathrm{V}}$Ru$^{\mathrm{VI}}$O$_{12}$ [10], their magnetic properties have been less explored, despite the interesting phenomena observed in other Ru(V)-containing oxides [11–17]. The interest in ruthenates is part of a wider focus on the magnetism of $4d$ and $5d$ oxides, which differ considerably from the more widely studied $3d$ oxides when effects such as strong spin-orbit coupling are considered [18]. Recently, some of us reported the synthesis of some new ruthenium(V) oxides using solution chemistry, among which was the hitherto unreported SrRu$_2$O$_6$ [19]. This adopts the PbSb$_2$O$_6$-type structure, consisting of two oxygen layers in a hexagonal unit cell, with Ru occupying 2/3 of voids within one layer, while Sr occupies 1/3 voids in the second layer. Powder neutron diffraction data collected at room temperature on SrRu$_2$O$_6$ showed that the Ru(V) moments are antiferromagnetically ordered at room temperature in both the basal plane and along the principal axis, hexagonal type II, akin to G-type antiferromagnetic ordering in cubic lattices [20]. Herein we present powder neutron diffraction data from SrRu$_2$O$_6$ over the range $7.5{-}623\,\mathrm{K}$ to determine experimen-

tally its Néel temperature, together with an investigation of electrical conductivity, and comprehensive calculations to examine the origin of electronic and magnetic properties.

II. EXPERIMENTAL AND COMPUTATIONAL METHODS

A polycrystalline sample of SrRu$_2$O$_6$ was prepared hydrothermally at 200 °C [19]. Magnetization was measured as a function of temperature using a Quantum Design MPMS-XL squid magnetometer with a furnace insert. Variable-temperature powder neutron diffraction data were collected using the WISH diffractometer (ISIS, UK) upon heating from 7.5 to 623 K. The sample was loaded into a thin vanadium can (8 mm diameter) placed at the end of a stick which was placed into a closed cycle refrigerator (CCR). The end of the stick comprised a ceramic block, a copper block with sensors, and heaters, and the sample was surrounded by two heat shields, essentially providing a minifurnace from the ceramic block. For operation between 7.5 and 300 K, the whole assembly was set in exchange gas. For temperatures above room temperature, the CCR head was kept at 300 K, the exchange gas pumped out, and the minifurnace was used. Rietveld analysis was performed using the GSAS software [21]. To make resistivity measurements, a small amount of sample was suspended in ethanol and sonicated before being deposited onto a thermally oxidized silicon wafer containing prepatterned metallic electrodes. A crystal was connected to the electrodes by focused-ion-beam–induced deposition (FIBID) of Pt [22] and four-probe *in-situ* measurements were made. An x-ray photoelectron spectroscopy (XPS) spectrum was recorded using a Kratos Axis Ultra DLD spectrometer with the samples attached to electrically conductive carbon tape, mounted on to a sample bar and studied at a base pressure of $\sim 2 \times 10^{-10}$ mbar at room temperature. The electronic structure of SrRu$_2$O$_6$ was calculated using density functional theory (DFT) with the HSE06 functional [23]

————————
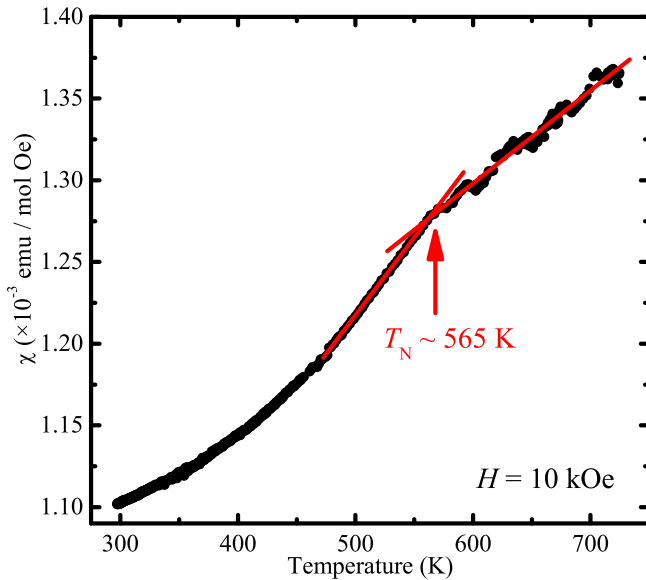*Author to whom correspondence should be addressed: r.i.walton@warwick.ac.uk

FIG. 1. (Color online) Magnetic susceptibility vs temperature for SrRu$_2$O$_6$ with the Néel temperature indicated. The red lines are linear interpolations of the data indicating a change in the slope of $\chi(T)$ at a Néel temperature of $\sim$565 K.
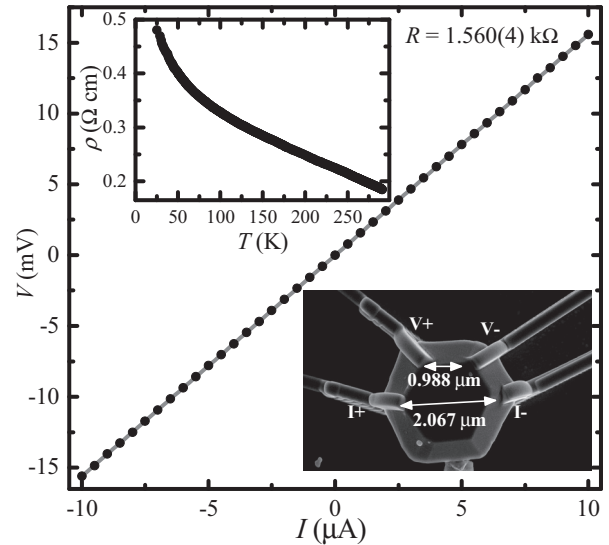

FIG. 2. Voltage-current plot of a single crystal of SrRu$_2$O$_6$ (shown lower-right inset); experimental error bars are smaller than data points, but note that the absolute value of resistance has a large uncertainty due to the size determination of the crystallite. Resistivity as a function of temperature is plotted in the upper left.

as implemented in the VASP code [24,25]. The projector-augmented wave (PAW) [26] method was used to describe the interactions between the cores (Sr:[Kr], Ru:[Kr], and O:[He]) and the valence electrons. HSE06 has been shown to yield improved descriptions of structure, band-gap, and defect properties of a number of oxide semiconductors and transition-metal oxides. Convergence with respect to k-point sampling and plane-wave energy cutoff were checked, and a cutoff of 750 eV and a k-point density of 0.2 k-points per Å were found to be sufficient. Calculations were deemed to be converged when the forces on all the atoms were less than 0.01 eV Å^{-1}.

Magnetic ordering, using a conventional unrestricted collinear spin model that implements symmetry broken solutions, was explored by constructing hexagonal and orthorhombic supercells containing four Ru ions with differing nearest-neighbor antiferromagnetic (AFM) and ferromagnetic (FM) spin alignments: AFM ordering (G type); FM ordering (F type); FM intralayer and AFM interlayer (A type); AFM intralayer and FM interlayer (C type); one AFM and two FM interactions intralayer for each Ru ("collinear AFM" within layers) and FM interlayer (labeled U type); and two AFM and one FM interactions intralayer for each Ru and FM interlayer (labeled V type). U type can be visualized as FM stripes along the a axis that are AFM connected intralayer and FM interlayer, whereas V type are AFM stripes FM connected intra- and interlayer.

III. RESULTS AND DISCUSSION

Figure 1 shows the magnetic susceptibility χ recorded with temperature T. Above room temperature the susceptibility increases with increasing temperature, with a discontinuity at $\sim$565 K corresponding to the Néel temperature and a linear

temperature dependence above T_N up to the maximum temperature measured. A similar linear $\chi(T)$ behavior has been observed in the charge-ordered antiferromagnet Na$_{0.5}$CoO$_2$ [27], in underdoped La$_{2-x}$Sr$_x$CuO$_4$ [28], and in several iron-based superconductors [29,30] in the high-temperature paramagnetic state. The susceptibility for SrRu$_2$O$_6$ at 400 K is much larger than the $\sim$10^{-4} emu mol^{-1} Oe^{-1} observed in the $3d$ La$_{2-x}$Sr$_x$CuO$_4$ but comparable with the susceptibility observed in Na$_{0.5}$CoO$_2$ and the iron pnictides. In the last materials this is attributed to the coexistence of both local moments and itinerant electrons [29,30].

The decomposition temperature (673 K [19]) of SrRu$_2$O$_6$ precludes the preparation of a thermally densified pellet for transport property measurements and hence the conductivity of a single, micron-scale crystal selected from the polycrystalline sample was measured. The measured voltage shows a clear linear dependence with current, and a resistance of the crystal of 1.560(4) kΩ was obtained (Fig. 2). By approximating the crystal shape and contact geometry to a cuboid (length $l = 0.99\,\mu$m, width $w = 1.60\,\mu$m, thickness $t = 0.92\,\mu$m), we estimate a resistivity ρ of $2.33 \times 10^5\,\mu\Omega$ cm. By an identical procedure, the ρ of a second crystal was found to have a value on the same order of magnitude, $1.03 \times 10^5\,\mu\Omega$ cm. The resistivity as a function of temperature, measured from the first crystal, further confirms that SrRu$_2$O$_6$ is a semiconductor (Fig. 2, inset). By using this van der Pauw configuration [31], it was also possible to obtain a value for the Hall coefficient R_H, of 6.098×10^{-6} m^3 C^{-1}, indicative of a p-type semiconductor, with a hole density p of 1.025×10^{18} cm^{-3}. In this configuration it is expected that the Hall voltage error is below 5% [32]. To understand these results, the electronic structure of SrRu$_2$O$_6$ was calculated. This confirmed the material to be semiconducting in nature, with a predicted band gap of 2.15 eV [Fig. 3(a)]. The valence band of the material
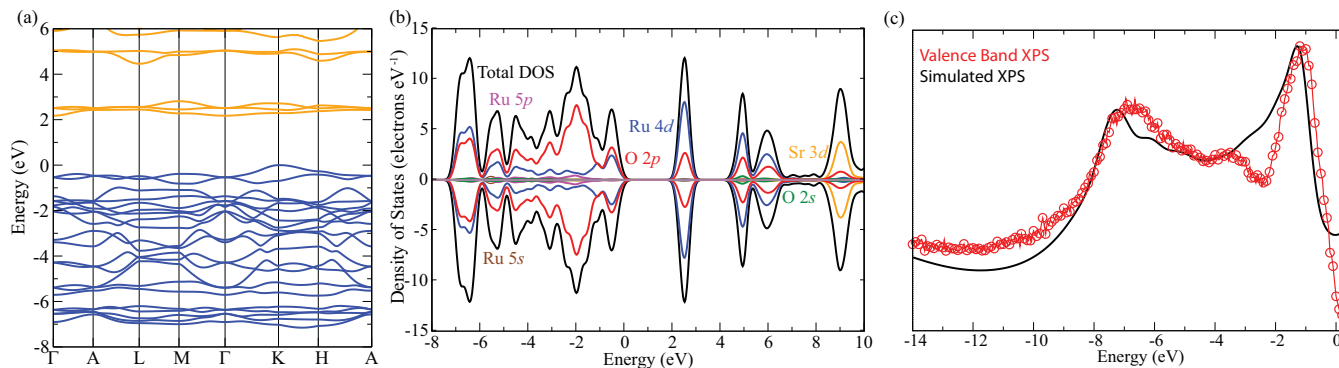
FIG. 3. (Color online) Calculated electronic structure of SrRu$_2$O$_6$ (a) band structure, (b) density of states with partial contributions in two spin channels, and (c) simulated XPS overlaid on the experimental XPS spectra. All were calculated using the G-type magnetic order found experimentally.
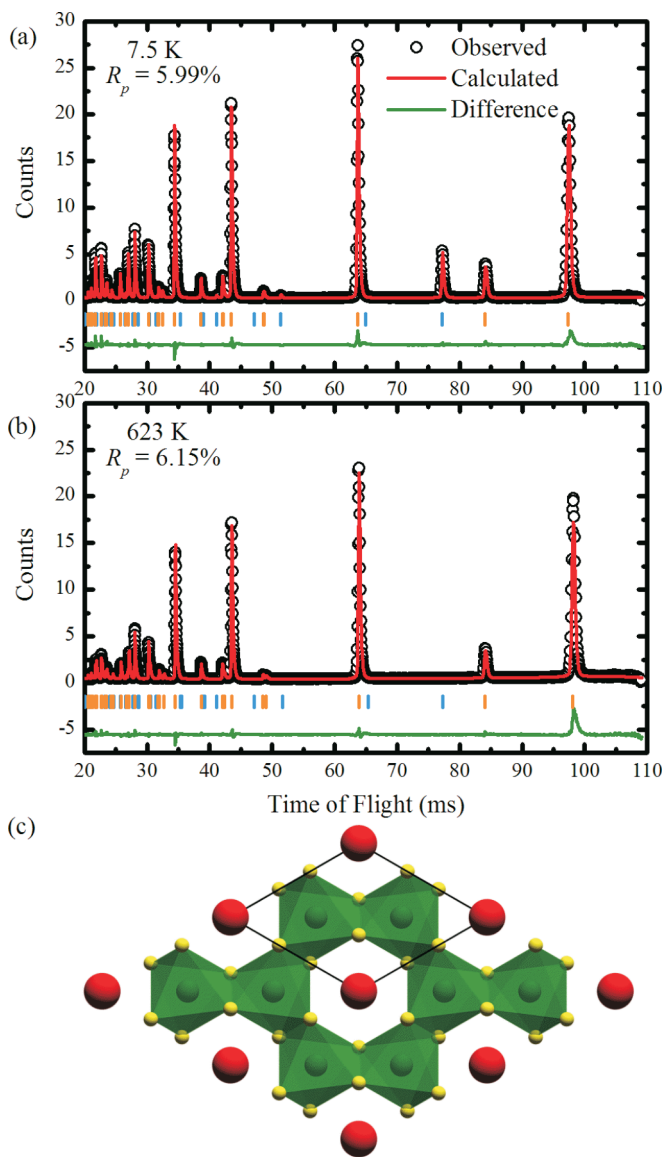

FIG. 4. (Color online) Rietveld fits of powder neutron data from SrRu$_2$O$_6$ (a) at 7.5 K and (b) at 623 K, and (c) a representation of the atomic structure of the material with green octahedra representing Ru and Sr shown as red spheres. In (a) and (b) blue ticks are due to the magnetic unit cell and orange due to the atomic unit cell.

displays pronounced O 2p and Ru 4d hybridization, while the conduction band minimum is dominated by unoccupied Ru 4d states, mixed with some O 2p states [Fig. 3(b)]. To compare our calculated results with experiment, we have overlaid simulated XPS data (constructed from the ion decomposed density of states weighted using the scattering cross sections
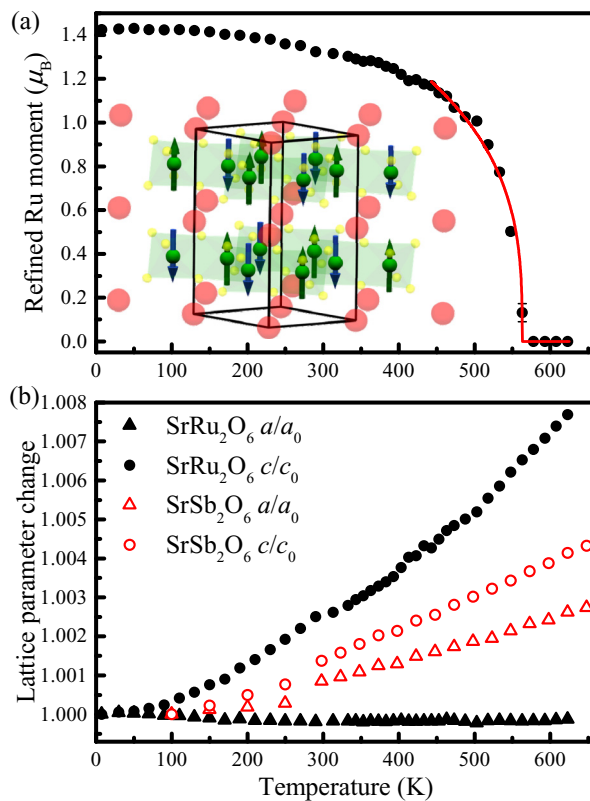

FIG. 5. (Color online) (a) Ru(V) moment and (b) normalized lattice constants (divided by the lattice constants at 7.5 K) of SrRu$_2$O$_6$ as a function of temperature. In (a) the red line is the fitted power law from 430 K used to determined T_N. Lattice constants of nonmagnetic SrSb$_2$O$_6$ as a function of temperature included (measured with laboratory powder x-ray diffraction and normalized to values at 100 K). Points on both plots without error bars have standard deviations smaller than the data points. Inset shows the magnetic cell, with red Sr^{2+} ions, yellow O^{2-} ions, and antiferromagnetically ordered Ru^{5+} ions in green.

TABLE I. Refined structural and magnetic parameters for $SrRu_2O_6$ from Rietveld refinement of powder neutron diffraction data at two temperatures (see Fig. 4 for Rietveld plots).

Refined parameter	$T = 7.5$ K	$T = 623$ K
a(Å)	5.20652(3)	5.20586(3)
c(Å)	5.22173(6)	5.26186(6)
Scale factor	399.0(6)	359.7(5)
R_p (%)	5.99	6.15
R_{wp} (%)	6.31	5.20
χ^2	15.56	10.66
U_{iso}(Sr), (Å^2)	0.0120(4)	0.0280(5)
Ru moment, μ_B	1.43(1)	-
U_{iso}(Ru), (Å^2)	0.0097(3)	0.0190(3)
x(O)/a	0.3789(1)	0.3791(1)
z(O)/c	0.2984(2)	0.2982(2)
U_{iso}(O), (Å^2)	0.0113(2)	0.0257(2)

of Yeh and Lindau [33]) over the experimental valence band spectrum in Fig. 3(c); the agreement between the two spectra corroborates the accuracy of our computational approach.

Figure 4 and Table I show the results of Rietveld refinement of atomic and magnetic structure refinements against powder neutron diffraction data at temperature above and below the magnetic ordering temperature. The atomic structure is refined using the expected $P\bar{3}1m$ space group for the $PbSb_2O_6$

structure, with no evidence for any structural phase transition over the temperature range studied, while the magnetic structure was solved using the $P\bar{3}1c$ space group, revealing an arrangement of spins such that there is antiferromagnetic order both within and between layers [Fig. 5(a) inset], analogous to G-type order in a cubic unit cell (hexagonal type II, according to the classification by Goodenough [20]). The ordered Ru^{5+} moment in $SrRu_2O_6$, refined against *in-situ* powder neutron diffraction data, was determined to be 1.425(10)μ_B at 7.5 K [34]. This moment is significantly smaller than the spin-only value for a d^3 ion (3.87μ_B), though it is comparable to values obtained in other Ru^{5+} ions in oxides [14,17], which may be ascribed to some degree of covalency in M-O bonds in $4d$ metal oxides [35]. The evolution of the ordered moment as a function of temperature, determined by Rietveld refinement, is shown in Fig. 5(a). The intensity of the magnetic Bragg peaks shows a loss in long-range magnetic ordering with a T_N of $\sim$570 K. Fitting with a power law [36] for the data above 440 K gives $T_N = 563(2)$ K. The ordering temperature is less than 100 K from the decomposition temperature of the material and is unusually high for a $4d$ oxide; to our knowledge the only $4d$ oxide with a higher reported T_N is the perovskite $SrTcO_3$, also containing a $4d^3$ magnetic ion, with a value of $\sim$1023 K [37].

Refinement of the lattice parameters of $SrRu_2O_6$ from the time-of-flight powder neutron diffraction data collected at temperatures from 7.5 to 623 K shows that while the c axis increases with temperature, the a axis displays a slight
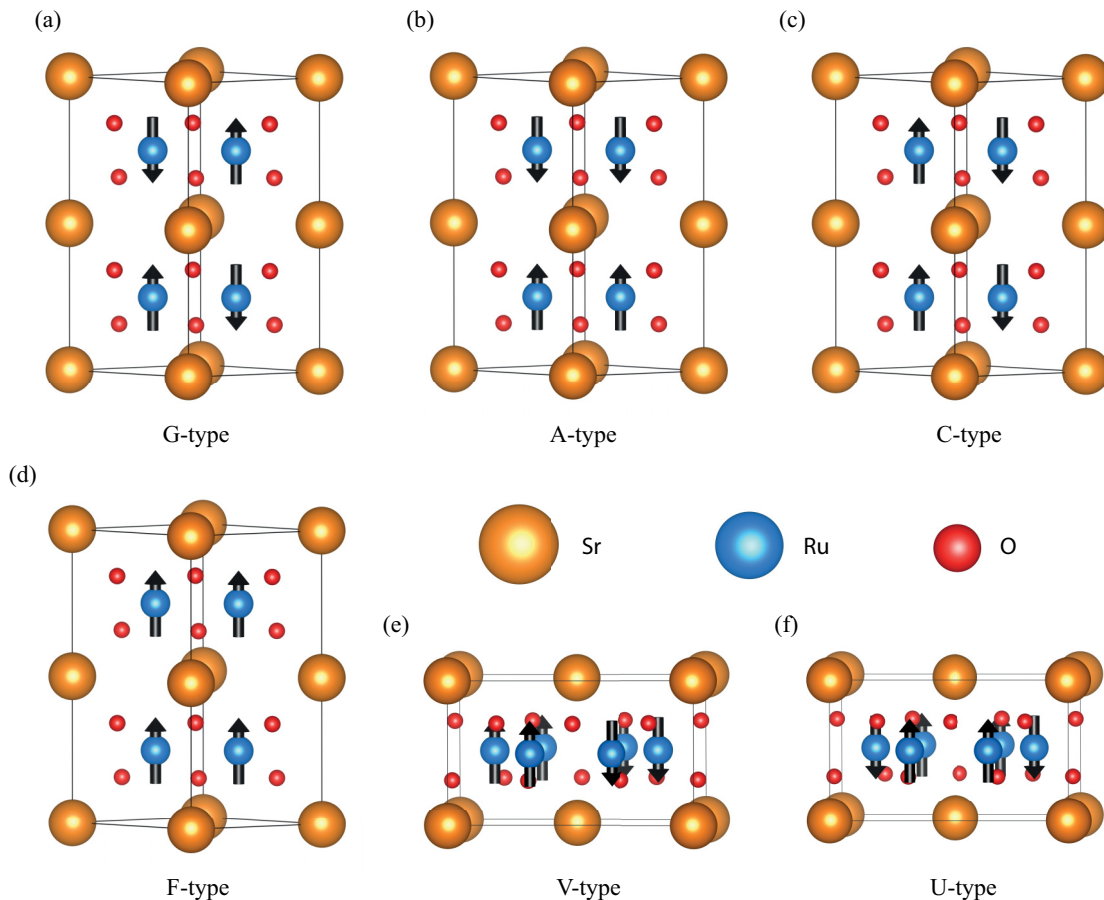

FIG. 6. (Color online) Spin configurations used in the DFT calculations (see text for explanation),

TABLE II. Relative energies (per four Ru atoms) of the different spin configurations tested for $SrRu_2O_6$. The alternative spin arrangements are all calculated at fully HSE06 relaxed geometries for each spin configuration, fixed geometries of the HSE06 relaxed G-type structure, and fixed to the experimentally reported room temperature structure.

Configuration	Fully relaxed (eV)	HSE06 G-type structure (eV)	Expt. geometry (eV)
G	0.000	0.000	0.000
A	0.457	0.602	0.624
C	0.002	0.002	0.002
F	0.461	0.614	0.638
U	0.138	0.194	0.202
V	0.281	0.385	0.404

decrease from 5.206 52(4) Å at 7.5 K to 5.205 60(3) Å at 313 K, and remains constant from 313 K up to 623 K [Fig. 5(b)]. For comparison, we examined $SrSb_2O_6$ as a diamagnetic analog with similar reduced mass: this displays linear thermal expansion in both the a and c axes from 100 to 648 K [Fig. 5(b)]. This anisotropic thermal expansivity of $SrRu_2O_6$ may be attributed to magnetoelastic coupling of the Ru(V) ions in the a-b plane, since the Ru–Ru intralayer distance remains constant over the whole temperature range studied. Since this behavior persists above T_N, it is possible that strong intralayer coupling on a local scale is present above the transition temperature which maintains the anisotropic expansivity.

The electronic structure calculations suggest that a distinct hybridization between the Ru and O states encourages electron transfer between Ru centers *via* O following a classical superexchange mechanism. Magnetic ordering was explored by constructing hexagonal and orthorhombic supercells containing four Ru ions (see Fig. 6) with differing nearest-neighbor AFM and FM spin alignments. Crucially, the G-type AFM ordering found by powder neutron diffraction proved to be the most energetically favorable. The relative stabilities of the different spin configurations are given in Table II.

Assuming a classical spin-3/2 Heisenberg Hamiltonian description:

$$H = \sum_{k=1}^{4} J_k \sum_{\langle i,j \rangle^k} \underline{S}_i \cdot \underline{S}_j, \qquad (1)$$

where $\underline{S}_i$ is the spin on the Ru atom, and J_k is the strengths of interaction between the kth nearest neighbors. In particular, J_1 is the strength of interaction between nearest-neighboring Ru atoms within a honeycomb layer, which favors lattice antiferromagnetic behavior; J_2 involves second nearest neighbors within each hexagonal ring and opposes the effect of J_1; J_3 characterizes the interaction between honeycomb layers; and finally J_4 includes interactions between Ru atoms on opposite corners of hexagonal rings and reinforces the effect of J_1. Therefore, the model can be described as a parallel set of interacting "honeycomb J_1-J_2-J_3 systems" (2D hexagonal lattice of spins with J_1, J_2, and J_4 interactions) [38,39]. We have performed classical Monte Carlo (MC) simulations, as implemented within the program SPINNER [40], of 11 honeycomb layers of 21×21 spins. 250,000 MC steps

were performed at each temperature after thermalizing, from 1200 K down to 0 K with a step of 5 K. The SPINNER code uses energy units of J_1 and allows for a maximum of three types of interactions; therefore, a number of simulations were conducted for different combinations of couplings to establish the effect of J_2/J_1, J_3/J_1, and J_4/J_1.

We considered coupling constants for three sets of geometries: DFT-optimized G-type spin configuration, fully optimized for each spin alignment, and experimental, obtained at room temperature. Using the differences between our calculated total hybrid DFT energies for G-, F-, A-, U-, and V-type ordering (Table II), we obtained $J_1 = 575$ K (428 and 599 K), $J_2/J_1 = 0.0291$ (0.0424 and 0.0275), $J_3/J_1 = 0.0287$ (0.0339 and 0.0330), and $J_4/J_1 = 0.0120$ (0.0169 and 0.0048) for G-type relaxed (fully relaxed and fixed) geometries. All interactions favor AFM between respective neighbors. Scaled by J_1 the phase transition between AFM G-type and a paramagnetic phase can be seen as a discontinuity in the slope of magnetic susceptibility with temperature, $d\chi/dT$. The statistical noise in our data made it difficult to accurately determine the critical temperature (Néel temperature, T_N). Therefore, the magnetic susceptibility simulated data have been filtered using moving averages over nine neighboring sample points, and we used the peak in the constant volume
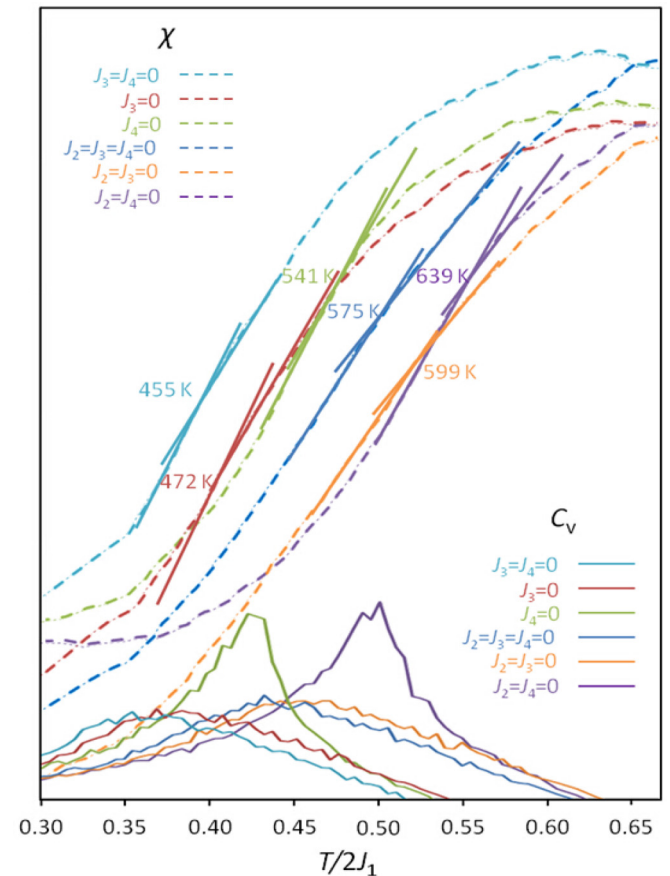

FIG. 7. (Color online) Magnetic susceptibility and constant volume heat capacity data obtained from Monte Carlo simulations. The curves are obtained under different simplified models highlighted in the key and explained in the text. The factor of 2 in the scaling of temperature (energy) accounts for the double counting in the lattice sums.

specific heat capacity (C_v) as a guide to where the discontinuity in χ lies (see Fig. 7).

First we considered interaction only between nearest neighbors ($J_2 = J_3 = J_4 = 0$, dark blue curve in Fig. 7) and found the critical temperature at approximately 575 K, which is an artificial feature characteristic of the current simulation parameters (supercell size and statistics) and is notably in contravention of the Mermin-Wagner theorem. Using only J_1 and J_3, the real Nel temperature 1.11 J_1 emerges. Indeed upon inclusion of interlayer interactions (nonzero J_3), which corresponds to a transition from a two-dimensional to a three-dimensional lattice of spins, we observed a significant enhancement of a peak in the C_v curve accompanied by a shift of the critical temperature to higher temperatures by 64 K for $J_3/J_1 = 0.033\,9$, which yields a maximum critical temperature of $T_N = 639$ K when $J_1 = 575$ K. Switching on additional intralayer interactions J_2 in turn weakens the AFM ordering and lowers T_N, whereas including J_4 interactions increases T_N.

The AFM ordering (exchange interaction) within the layers is much stronger than between them, consistent with the much shorter Ru–Ru distance in the layers. The small value of J_3 also explains the high stability (a low value of the relative energy) of the metastable C phase. The values of our calculated coupling constants J_k are also consistent with the ground-state AFM arrangement both in classical and quantum mechanical phase diagrams for the "honeycomb J_1-J_2-J_3 system" [38,39]. Using the first set of coupling constants that characterize interactions in the DFT-optimized G-type ordered phase, we estimate the Néel temperature to be 564 ± 5 K, very close to the experimentally measured value, whereas if we use the third set of coupling constants, obtained for the atomic structure that is fixed to that experimentally observed, then we estimate a slightly higher Néel temperature of 594 K. (The values are obtained by extrapolating the critical temperatures from two cases, $J_4 = 0$ and $J_2 = 0$.)

Previous examples of high-temperature magnetic ordering in 4d and 5d oxides have been restricted to materials with three-dimensional structures, such as the 5d perovskites SrTcO$_3$ [37], NaOsO$_3$ [41], and Sr$_2$CrOsO$_6$ [42] (the last being ferromagnetic). Interestingly, three-dimensional antiferromagnetic order in the layered PbSb$_2$O$_6$ structure has also been seen for the materials MAs$_2$O$_6$, $M =$ Mn, Co, Ni, and Pd [43,44], with PdAs$_2$O$_6$ showing a Néel temperature T_N of 140 K [45], but the magnetic ions here sit on the A site of the structure, with greater interatomic separation from their magnetic neighbors than the B-site Ru in SrRu$_2$O$_6$. Our observation of high-temperature, three-dimensional magnetic order in a two-dimensional, semiconducting material provides a structurally distinct system for further study of the magnetism and electronic structure in 4d oxides, with the possibility of preparation of doped or 5d analogs of SrRu$_2$O$_6$.

Note added. We note that during the preparation of this article, Singh has published a theoretical study of SrRu$_2$O$_6$ using density functional theory [46] and has independently confirmed that magnetic anisotropy is high in this system, with comparable energy scales for moment formation and ordering which favors moments oriented along the c axis. In addition, Wang *et al.* have reported theoretical studies of the SrRu$_2$O$_6$ that replicate the antiferromagnetic order and provide evidence for strong spin-orbit coupling of Ru atoms [47]. Tian *et al.* have also published a powder neutron diffraction and magnetisation study of SrRu$_2$O$_6$, along with DFT and Monte Carlo simulations, and find similar results to our work [48].

[1] J. M. Longo, P. M. Raccah, and J. B. Goodenough, J. Appl. Phys. **39**, 1327 (1968).

[2] Y. Noro and S. Miyahara, J. Phys. Soc. Jpn. **27**, 518A (1969).

[3] K. Ishida, H. Mukuda, Y. Kitaoka, K. Asayama, Z. Q. Mao, Y. Mori, and Y. Maeno, Nature (London) **396**, 658 (1998).

[4] A. Tamai, M. P. Allan, J. F. Mercure, W. Meevasana, R. Dunkel, D. H. Lu, R. S. Perry, A. P. Mackenzie, D. J. Singh, Z. X. Shen, and F. Baumberger, Phys. Rev. Lett. **101**, 026407 (2008).

[5] C. Lester, S. Ramos, R. S. Perry, T. P. Croft, R. I. Bewley, T. Guidi, P. Manuel, D. D. Khalyavin, E. M. Forgan, and S. M. Hayden, Nat. Mater. **14**, 373 (2015).

[6] Z. Q. Mao, M. Zhou, J. Hooper, V. Golub, and C. J. O'Connor, Phys. Rev. Lett. **96**, 077205 (2006).

[7] G. Cao, L. Balicas, W. H. Song, Y. P. Sun, Y. Xin, V. A. Bondarenko, J. W. Brill, S. Parkin, and X. N. Lin, Phys. Rev. B **68**, 174409 (2003).

[8] C. Renard, S. Daviero-Minaud, and F. Abraham, J. Solid State Chem. **143**, 266 (1999).

[9] C. Dussarrat, J. Fompeyrine, and J. Darriet, Eur. J. Solid State Inorg. Chem. **32**, 3 (1995).

[10] C. Renard, S. Daviero-Minaud, M. Huve, and F. Abraham, J. Solid State Chem. **144**, 125 (1999).

[11] P. D. Battle and W. J. Macklin, J. Solid State Chem. **52**, 138 (1984).

[12] J. Darriet, F. Grasset, and P. D. Battle, Mater. Res. Bull. **32**, 139 (1997).

[13] K. E. Stitzer, M. D. Smith, W. R. Gemmill, and H.-C. zur Loye, J. Am. Chem. Soc. **124**, 13877 (2002).

[14] N. G. Parkinson, P. D. Hatton, J. A. K. Howard, C. Ritter, F. Z. Chien, and M.-K. Wu, J. Mater. Chem. **13**, 1468 (2003).

[15] H. Sato, T. Watanabe, and J.-I. Yamaura, Solid State Commun. **131**, 707 (2004).

[16] T. Munenaka and H. Sato, J. Phys. Soc. Jpn. **75**, 103801 (2006).

[17] P. Manuel, D. T. Adroja, P.-A. Lindgard, A. D. Hillier, P. D. Battle, W.-J. Son, and M.-H. Whangbo, Phys. Rev. B **84**, 174430 (2011).

[18] W. Witczak-Krempa, G. Chen, Y. B. Kim, and L. Balents, Ann. Rev. Condens. Matt. Phys. **5**, 57 (2014).

[19] C. I. Hiley, M. R. Lees, J. M. Fisher, D. Thompsett, S. Agrestini, R. I. Smith, and R. I. Walton, Angew. Chem. Int. Ed. **53**, 4423 (2014).

[20] J. B. Goodenough, *Magnetism and the Chemical Bond* (John Wiley and Sons, New York, 1963).

[21] A. C. Larson and R. B. Von Dreele, General Structure Analysis System (GSAS), Los Alamos National Laboratory Report LAUR 86–748 (2000).

[22] J. M. De Teresa, R. Cordoba, A. Fernandez-Pacheco, O. Montero, P. Strichovanec, and M. R. Ibarra, J. Nanomaterials **2009**, 936863 (2009).

[23] A. V. Krukau, O. A. Vydrov, A. F. Izmaylov, and G. E. Scuseria, J. Chem. Phys. **125**, 224106 (2006).

[24] G. Kresse and J. Furthmuller, Phys. Rev. B **54**, 11169 (1996).

[25] G. Kresse and J. Hafner, Phys. Rev. B **49**, 14251 (1994).

[26] P. E. Blochl, Phys. Rev. B **50**, 17953 (1994).

[27] M. L. Foo, Y. Y. Wang, S. Watauchi, H. W. Zandbergen, T. He, R. J. Cava, and N. P. Ong, Phys. Rev. Lett. **92**, 247001 (2004).

[28] T. Nakano, M. Oda, C. Manabe, N. Momono, Y. Miura, and M. Ido, Phys. Rev. B **49**, 16000 (1994).

[29] X. F. Wang, T. Wu, G. Wu, H. Chen, Y. L. Xie, J. J. Ying, Y. J. Yan, R. H. Liu, and X. H. Chen, Phys. Rev. Lett. **102**, 117005 (2009).

[30] J. Q. Yan, A. Kreyssig, S. Nandi, N. Ni, S. L. Bud'ko, A. Kracher, R. J. McQueeney, R. W. McCallum, T. A. Lograsso, A. I. Goldman, and P. C. Canfield, Phys. Rev. B **78**, 024516 (2008).

[31] L. J. van der Pauw, Philips Res. Rep. **13**, 1 (1958).

[32] R. Chwang, B. J. Smith, and C. R. Crowell, Solid-State Electron. **17**, 1217 (1974).

[33] J. J. Yeh and I. Lindau, At. Data Nucl. Data Tables **32**, 1 (1985).

[34] In a previous report by some of the authors of this article the magnetic moment was incorrectly reported due to an error in the implementation of crystallographic symmetry operations in the software used in that work [19].

[35] J. Hubbard and W. Marshall, Proc. Phys. Soc. **86**, 561 (1965).

[36] S. Blundell, *Magnetism in Condensed Matter* (Oxford University Press, Oxford, UK, 2001).

[37] E. E. Rodriguez, F. Poineau, A. Llobet, B. J. Kennedy, M. Avdeev, G. J. Thorogood, M. L. Carter, R. Seshadri, D. J. Singh, and A. K. Cheetham, Phys. Rev. Lett. **106**, 067201 (2011).

[38] J. B. Fouet, P. Sindzingre, and C. Lhuillier, Eur. Phys. J. B **20**, 241 (2001).

[39] J. Reuther, Doktors der Naturwissenschaften, Karlsruher Instituts für Technologie, 2011.

[40] M. A. D. Vries, Spinner, A Classical Monte Carlo Spin Lattice Simulation Program, http://www.ccp5.ac.uk (2007).

[41] Y. G. Shi, Y. F. Guo, S. Yu, M. Arai, A. A. Belik, A. Sato, K. Yamaura, E. Takayama-Muromachi, H. F. Tian, H. X. Yang, J. Q. Li, T. Varga, J. F. Mitchell, and S. Okamoto, Phys. Rev. B **80**, 161104(R) (2009).

[42] Y. Krockenberger, K. Mogare, M. Reehuis, M. Tovar, M. Jansen, G. Vaitheeswaran, V. Kanchana, F. Bultmark, A. Delin, F. Wilhelm, A. Rogalev, A. Winkler, and L. Alff, Phys. Rev. B **75**, 020404 (2007).

[43] A. M. Nakua and J. E. Greedan, J. Solid State Chem. **118**, 402 (1995).

[44] D. Orosel and M. Jansen, Z. Anorg. Allg. Chem. **632**, 1131 (2006).

[45] M. Reehuis, T. Saha-Dasgupta, D. Orosel, J. Nuss, B. Rahaman, B. Keimer, O. K. Andersen, and M. Jansen, Phys. Rev. B **85**, 115118 (2012).

[46] D. J. Singh, Phys. Rev. B **91**, 214420 (2015).

[47] D. Wang, W.-S. Wang, and Q.-H. Wang, Phys. Rev. B **92**, 075112 (2015).

[48] W. Tian, C. Svoboda, M. Ochi, M. Matsuda, H. B. Cao, J.-G. Cheng, B. C. Sales, D. G. Mandrus, R. Arita, N. Trivedi, and J.-Q. Yan, Phys. Rev. B **92**, 100404 (2015).